Research article

Pulsed electroplating of ZrO$_2$-reinforced Ni-Cr alloy coatings from the duplex complexing agents-containing bath for engineering applications: Importance of operating conditions

Mir Saman Safavi [*], Sima Soleimanzadeh Ghazijahani, Ali Rasooli [**]

Department of Materials Engineering, Faculty of Mechanical Engineering, University of Tabriz, Tabriz, Iran

A B S T R A C T

The progress in tribocorrosion performance of the engineering parts is in dire need of improving their surface properties. In the present contribution, Ni-Cr-ZrO$_2$ layers were electrodeposited on St37 steel. The stress was put on optimizing the process factors, including the parameters involved in pulsed current electrodeposition and level of the ZrO$_2$ reinforcing nanoparticles (0–20 g/L) in the bath. The surface characteristics of the electrodeposits were evaluated using FESEM, EDS, AFM, and XRD. The tribomechanical characteristics of the films were determined using a Vickers microhardness tester and pin-on-disk apparatus. The electrochemical behavior of the samples was studied using OCP, EIS, PDP, and immersion techniques. The results demonstrated that the included ZrO$_2$ nanoparticles led to more homogenous, rougher, and defect-free surfaces, while they did not change the phase composition of the alloy electrodeposits. The polarization resistance of the Ni-Cr alloy coating increases by 6.7 times when 10 g/L of the reinforcing nanoparticles is added to the electrolyte. A decrease of $\approx$42 % in the mean COF value was obtained by the incorporation of 10 g/L ZrO$_2$ nanoparticles into the plating bath. The coating system developed holds the promise to address both technical requirements and health concerns.

1. Introduction

The increase in surface properties of the engineering materials is of prime significance since most of the environment-material interactions occur on the surface. The carbon steels are extensively used in various industrial applications, such as building, transportation, and pipelines. It is logical to promote the surface properties of carbon steel to widen its applications, particularly in harsh service conditions, such as marine environments. The application of appropriate coating technology and material can guarantee the success of surface modification applied [1–5].

A variety of wet and dry surface modification technologies have been developed to meet the R & D and industrial demands based on the properties expected and economic condition [6–11]. Among the wide spectrum of the coating techniques, electrodeposition garnered tremendous attention due to its unique pros, including low-cost, low-operating temperature, simplicity of operation, and ability to produce alloy, composite and multilayer films [12–19].

The electrodeposited Ni coatings have been the focus of numerous research due to their favorable tribomechanical and anti-

corrosion performance. The desired properties of these coatings can be further enhanced by the addition of optimum levels of appropriate alloying element(s) and reinforcing phase(s) [20–28]. The inclusion of less toxic Cr(III) alloying element in Ni electrodeposit seriously enhances its overall performance; However, the high internal stress originated from the sever hydrogen evolution in Cr(III)-containing electrolytes leads to poor surface quality of the film. Thus, it is essential to allow a precise control over the processing parameters, in particular the use of pulse electrodeposition and/or add appropriate complexing agents to ensure the formation of crack-free electrodeposits. Ni-Cr is a promising coating material, which can be utilized in a variety of the industrial and biomedical applications, e.g., automotive and dental prosthesis. Besides offering excellent mechano-corrosion performance, the lack of toxic Cr (VI)-containing salts in the electrolyte of this coating have diminished health risks. Moreover, the use of anionic surfactants, e.g., sodium dodecyl sulfate (SDS) at a controlled level, as well as biocompatible reinforcing agents, such as ZrO_2 and Nb_2O_5, may cause very low risk to human and environmental health [29–47]. It is worth mentioning that the overall performance of pure Cr(III) coating is not as high as the Cr(VI) layer [48]. The concept of composite coating allows the researcher to further rise the final properties of the material through the incorporation of proper concentrations of the reinforcing phases. A survey on the literature illustrates that several attempts have been made to increase the overall performance of the Ni-Cr alloy electrodeposits by inclusion of ceramic particles, such as TiO_2 [32], hBN [48], and Al_2O_3 [49], in the microstructure of the growing allot layer. ZrO_2 is a class of ceramic materials, suggesting high thermal resistance, chemical stability, mechanical properties, e.g., elastic modulus (100–250 GPa at 20 °C) and hardness (1220 HV), good biological properties, and outstanding wear resistance, therefore, has found different applications [50–54]. In light of the mentioned features, the application of ZrO_2 as a reinforcing agent for Ni-Cr electrodeposits may carry the promise of the fabrication of efficient protective layers.

In general, there are very limited in-depth R & D works devoted to improving the overall characteristics of Ni-Cr electrodeposits via simultaneous application of reinforcing agents and controlling operating conditions. Following from the gap in literature, the present contribution endeavors to promote the mechanical, corrosion, and tribological properties of the Ni-Cr coatings by the addition of ZrO_2 nanoparticles, optimizing processing factors, such as current density, duty cycle, and the use of duplex complexing agents, e.g., malonic acid and citric acid. It is believed that the strategy adopted can tackle the challenges facing the electrodeposition of crack-free Ni-Cr layers for potential use in engineering applications.

2. Materials and methods

2.1. Materials

The St37 steel sheet, containing 0.12 % carbon, measured 20 mm in length, 10 mm in width, and 3 mm in thickness, was used as a working electrode. The surface of the working electrode was pre-treated by 100–1000 grit SiC abrasive emery papers to eliminate possible oxides. Then, the sheets were successively immersed in acetone- and ethanol-containing beakers and placed in an ultrasonic bath for 20 min to remove pollution and greases. The surface of the sheets was further degreased and activated by plunging them into the 7 M NaOH for 10 min and 15 % (v/v) nitric acid for 12 s, respectively. The counter electrode material was Ni plate with the surface area of 800 mm^2 exposed to the electrolyte.

2.2. Electroplating procedure

A conventional two-electrode configuration in an electrochemical glass cell containing 250 mL of the electrolyte, where the
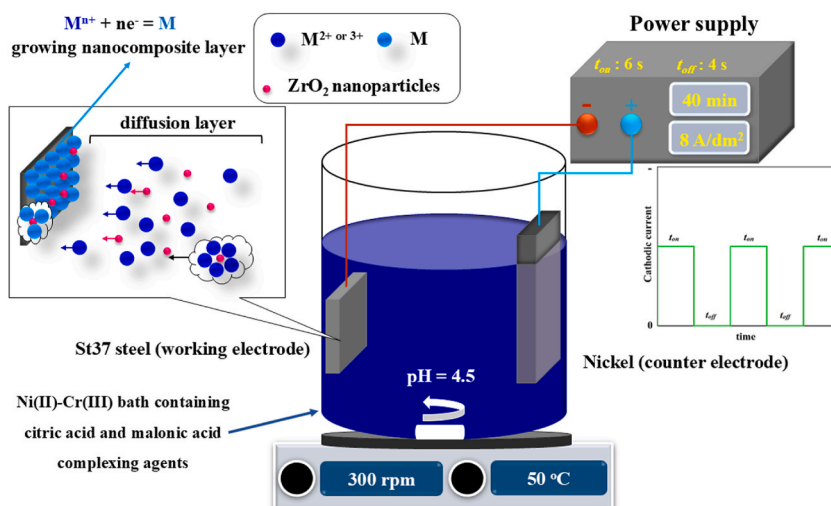

Fig. 1. Schematic illustration of the electrodeposition process and operating parameters adopted in the present study.

electrodes are vertically immersed, was employed. The interelectrode space was 40 mm. The employed operating parameters are schematically illustrated in Fig. 1. Besides, the chemical composition of the bath is outlined in Table 1. The electrolyte was prepared by dissolving the mentioned chemicals, one-by-one, in 250 mL distilled water.

The FESEM image of the as-purchased ZrO_2 nanoparticles is illustrated in Fig. 2. The image shows that the morphology of the nanoparticles is spheroidal. The particle size of the spheroidal ZrO_2 nanoparticles is in the range of 30–50 nm.

The use of duplex complexing agents, i.e., citric acid and malonic acid, in Ni(II)-Cr(III) bath leads to the inclusion of desired amounts of chromium in the growing electrodeposit. The ZrO_2-containing suspension was ultrasonically agitated for 10 min under the power of 150 W to guarantee the homogeneous dispersion of the nanoparticles throughout the plating bath. Electroplating process was performed under the pulse current mode to provide sufficient time for reduction of the ions on preferential sites over the surface of the working electrode. This strategy can lead to crack-free deposits. The electrolyte agitation suspended the nanoparticles in the electrolyte, avoided concentration polarization, contributed to the convection of the ions and nanoparticles towards the working electrode, and removed the generated H_2 bubbles from the surface of the working electrode. In the following text, the layers electroplated from the electrolytes comprising 0, 5, 10, and 20 g/L ZrO_2 nanoparticles will be labeled Ni-Cr, Ni-Cr-5Z, Ni-Cr-10Z, and Ni-Cr-20Z, respectively.

2.3. Characterization

XRD Cu-Kα radiation (Bruker D8 Advance, Germany) was utilized to determine the phase structure of the layers in the 2θ range of 10–90° with a step size of 0.02° and scanning speed of 1°/min. The crystallite size of the layers was measured using the Scherrer equation shown elsewhere [55].

Surface morphology and elemental composition of the Ni-Cr-based layers were assessed via the FESEM (MIRA 3 Tescan, Czech Republic) coupled with the EDS. The surface topography and roughness of the layers were studied using the AFM (Nanosurf, Switzerland).

The microhardness of the electrodeposits was determined by employing Vickers microhardness tester (Novotest T8- MCV, Ukraine) under a load of 10 g and a dwell time of 15 s. The values presented are the average of five measurements.

The corrosion performance of the Ni-Cr-based layers was determined by a potentiostat-galvanostat (Zive SP2, WonATech, South Korea) with a sinusoidal perturbation potential in the frequency window of 100 kHz to 10 mHz using the EIS. A three-electrode glass electrochemical cell comprising of the Ni-Cr-based coatings as the working electrode (WE), a rectangular platinum foil as the counter electrode (CE), and an aqueous saturated calomel electrode (SCE) as the reference electrode (RE) was utilized. The corrosive electrolyte was 3.5 % (w/v) NaCl solution. All of the corrosion tests were carried out at 25 ± 1 °C. ZSim™ software (Demonstration Version) was employed to fit the experimental data. The potentiodynamic polarization was done over the potential range of -300 to 400 mV *vs.* the OCP at a potential scan rate of 1 mV/s. The surface morphology of the corroded samples was studied using the FESEM (MIRA 3 Tescan, Czech Republic).

The electrodeposited coatings with the same surface area were plunged into 3.5 % (w/v) NaCl solution at 25.0 ± 1 °C for 14 days. Upon completion of the immersion period, the samples were processed following the procedure explained in our previous paper [1].

The wear tests were performed employing a pin-on-disc wear apparatus (*Tajhiz Sanat Nasr* Co., Iran) at 28 ± 1 °C and humidity of approx. 30 %. The pin used in the tests was an ASTM 52100 bearing steel with a diameter of 5 mm. The wear test parameters were set as follows: sliding distance of 100 m, sliding speed of 190 rpm, and vertical load of 2 N. Upon completion of the test, the specimens were treated as per the procedure addressed in our previous paper [1].

The procedure adopted for the statistical analysis was described in our previously published paper [1].

3. Results and discussion

3.1. Optimizing current density and duty cycle

The current density and duty cycle play a central role in electrodeposition of high-quality and defect-free coatings containing controlled levels of the homogeneously dispersed reinforcing particles. The importance of the application of optimized processing parameters is highlighted when electrodeposition of the coating materials that cause severe H_2 bubbles formation, e.g., Cr electrodeposits. Since improving the mechanical properties of the coatings is one of the primary purposes of the present work, the

Table 1
Chemical composition of the baths used for fabrication of the coatings.

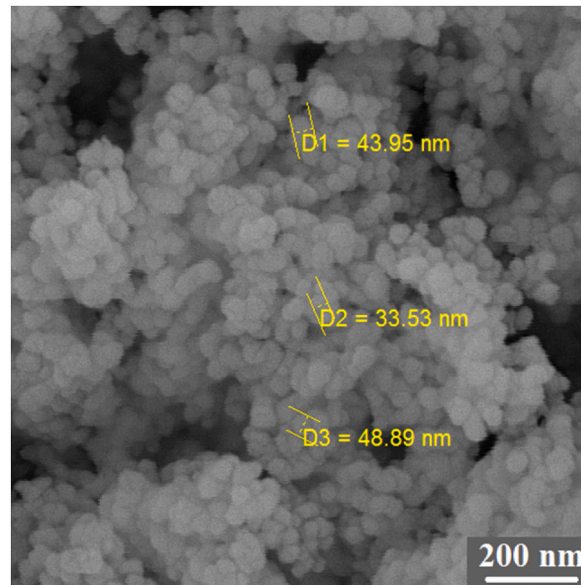| Chemicals	Concentrations in the bath (g/L)	Sourced from
$NiSO_4.6H_2O$	60	Merck
$CrCl_3.6H_2O$	85	Merck
H_3BO_3	50	Merck
$NiCl_2.6H_2O$	40	Merck
$C_6H_8O_7$	50	Sigma-Aldrich®
$C_3H_4O_4$	30	Sigma-Aldrich®
$NaC_{12}H_{25}SO_4$	0.3	Sigma-Aldrich®
ZrO_2	0–20	US Research Nanomaterials, Inc.

Fig. 2. FESEM image of the as-purchased ZrO_2 nanoparticles.

microhardness of the Ni-Cr layers electrodeposited at various current densities and duty cycles was measured and listed in Table 2 to obtain the best outcome from the mechanical point of view. Firstly, the microhardness of the coatings electrodeposited under the current density range of 2–8 A/dm^2 and a constant duty cycle of 60 % was measured, and the results illustrated that the application of 8 A/dm^2 yielded the highest microhardness. Then, the microhardness of this coating electroplated at a duty cycle range of 40–80 % was evaluated. Overall, the films electroplated under the current density of 8 A/dm^2 and duty cycle of 60 % offered the highest tribo-mechanical properties. The microhardness is an effective factor in determining the wear resistance of the material. Based on Archard's equation, the higher the microhardness, the higher the wear resistance is. Therefore, it can be concluded that the harder coatings may show higher wear resistance [56].

3.2. Phase analysis

The XRD diffractograms of the Ni-Cr-based coatings are exhibited in Fig. 3. The XRD diffractogram of the Ni-Cr coating contains Ni peaks at $2\Theta \approx 44°$, 52°, and 76° corresponding to (111), (200), and (220) crystallographic planes of the FCC lattice, respectively. Besides, two XRD peaks of Cr (110) and Cr (211) were detected at $2\Theta \approx 44°$ and 82°, respectively. The emergence of Ni and Cr XRD peaks at $2\Theta \approx 44°$ demonstrates the formation of Ni-Cr solid solution due to the partial dissolution of Cr in Ni. The absence of the peak related to the substrate confirms the formation of thick and dense coatings that uniformly cover the surface of the steel substrate. The electrodeposition of Ni and Cr from a Ni(II)-Cr(III) may be occurred through the following reactions [57]:

Trivalent Cr reduction to Cr (s)

$$Cr^{3+} + e^- \rightarrow Cr^{2+} \tag{1}$$

$$Cr^{2+} + 2e^- \rightarrow Cr \ (s) \tag{2}$$

Bivalent Ni reduction to Ni

Table 2
Microhardness values of the Ni-Cr coatings electrodeposited at various current densities and duty cycles.

Current density (A/dm^2)	Microhardness (HV)
2	420 ± 8
4	437 ± 10
6	486 ± 11
8	532 ± 9
Duty cycle (%)	**Microhardness (HV)**
40	510 ± 5
60	532 ± 9
80	506 ± 15

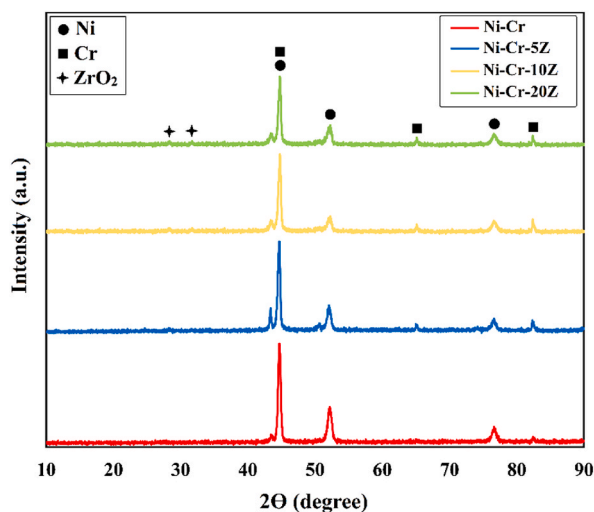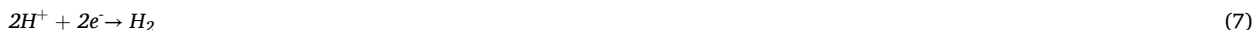**Fig. 3.** XRD diffractograms of the Ni-Cr-based electrodeposits containing various amounts of the ZrO_2 nanoparticles.

$$Ni2+ + X- \rightarrow NiX+ \tag{3}$$

$$NiX+ + e- \rightarrow NiX(ads) \tag{4}$$

$$NiX(ad_s) + e^- \rightarrow Ni + X^- \tag{5}$$

General hydrogen gas evolution

$$H_2O + 2e- \rightarrow H2 + 2OH- \tag{6}$$

$$2H^+ + 2e^- \rightarrow H_2 \tag{7}$$

It is to be mentioned that there might be several forms of Cr complexes, including $(Cr(H_2O)_6)^{3+}$ and $(Cr(H_2O)_5Cl)^{2+}$, when electroplating is carried out from Cr(III) bath. These complexes reduce to intermediate complexes, followed by being adsorbed on the cathode [57,58].

The differences observed in the XRD patterns of the nanocomposite coatings compared to that of Ni-Cr are the presence of Cr (200) XRD peak at $2\Theta \approx 44°$ and appearance of two low absolute intensity ZrO_2 XRD peaks at $2\Theta \approx 28°$ and 31°. It is to be noted that the ZrO_2 XRD peaks did not appear in the pattern of Ni-Cr-5Z film due to the low content of the included ZrO_2 nanoparticles in this film.

Besides a change in peak absolute intensity of the peak at $2\Theta \approx 44°$, the included nanoparticles affected the peak's width. This observation correlates with a change in the crystallite size of the coating studied. The crystallite size of the electrodeposits was calculated using the Scherrer equation and outlined in Table 3. A progressive decrease in the crystallite size of the Ni-Cr layer is observed with the addition of the nanoparticles up to 10 g/L. A further increase in the level of the nanoparticles in the electrolyte to 20 g/L leads to enlarged crystallites. The function of the included reinforcements in providing potential heterogeneous nucleation locations answers the question of why the crystallite size of the nanocomposite films is smaller than that of Ni-Cr one.

3.3. Surface morphology and topography

The thickness of the alloy and nanocomposite layers is in the range of 17–25 μm. The nanocomposite layers are thicker since the ZrO_2 nanoparticles are incorporated into the growing layer. Xu et al. [59] have shown that the co-deposition of ZrO_2 nanoparticles with Ni-Mo electrodeposits increases the thickness of the layers. The top-view FESEM images of the electrodeposits at different magnifications are illustrated in Fig. 4. The microstructure of the Ni-Cr layer consists of nodular and polyhedral grains (see Fig. 4a and

Table 3
The crystallite size of the coatings electroplated from electrolytes containing various levels of the ZrO_2 nanoparticles.

Coating type	Crystallite size (nm)
Ni-Cr	91
Ni-Cr-5Z	82
Ni-Cr-10Z	75
Ni-Cr-20Z	80

c). Fig. 4b) shows that there are micro-cracks all over the surface of the Ni-Cr, shown by the arrows. The FESEM images of the nanocomposite films in Fig. 4d–l), demonstrate the successful codeposition of the ZrO_2 nanoparticles with the alloy coating. According to Fig. 4e–h, and k) the included ZrO_2 nanoparticles are evenly distributed throughout the alloy matrix so that a non-continuous layer consisting of the ceramic nanoparticles covers the underlying Ni-Cr coating. A higher amount of ZrO_2 may be incorporated into the layer when the higher concentration of the nanoparticles is added to the electrolyte. There are aggregated nanoparticles over the surface of the Ni-Cr-20Z coating. The agglomeration of the nanoparticles leads to the formation of nanopores on the surface of Ni-Cr-20Z coating, illustrated by arrows in Fig. 4k) and l).

    Fig. 5a) and b) show the uniform distribution of the Zr and O throughout the surface of layers; However, agglomeration of the elements in specified parts of the surface can be observed in Fig. 5c), illustrating the destructive influence of the increased loadings of the ZrO_2 nanoparticles on the morphological features. Fig. 6 exhibits the 2D and 3D AFM images of the samples.
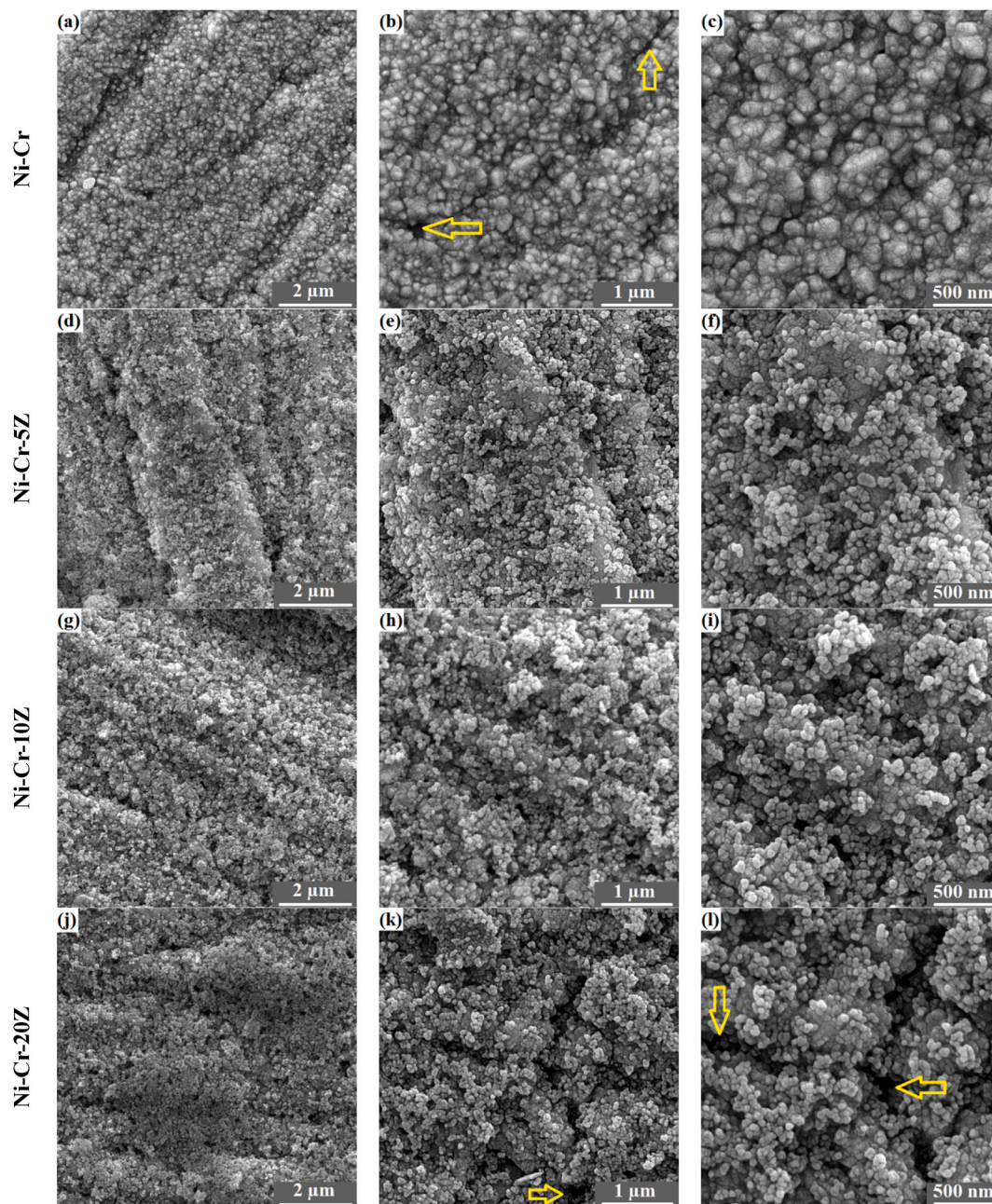

Fig. 4. The top-view FESEM images of the electrodeposits at various magnifications: (a–c): Ni-Cr, (d–f): Ni-Cr-5Z, (g–i): Ni-Cr-10Z, and (j–l): Ni-Cr-20Z.

Unlike the alloy electrodeposit, the surface morphology of the composite ones, in particular Ni-Cr-10Z, is compact and defect-less. EDS elemental mapping images of the Zr and O throughout the surface of nanocomposite layers are indicated in Fig. 5. The images further approve the codeposition of the ZrO_2 nanoparticles with the growing alloy electrodeposit.

The 2D AFM images in Fig. 6a–c, e, and g) demonstrate that there are a few micron-sized pore throughout the surface of the layers. 2D AFM images clearly show that the amount of surface defects, e.g., pores, diminishes in the nanocomposite coatings. According to 3D AFM images, presented in Fig. 6b–d, f, and h), the surface topography of the coatings studied comprises crests and valleys. The FESEM and AFM images presented in Figs. 4 and 6, respectively, show that the inclusion of the ZrO_2 nanoparticles in the Ni-Cr matrix led to a denser and rougher surface. The parameters acquired by elaborating AFM data are outlined in Table 4. The results show the enhanced level of the nanoparticles in the electrolyte leads to enhanced surface roughness, potentially due to the rough and hard nature of the included ZrO_2 nanoparticles [1].

3.4. Elemental composition

The changes in the content of Zr and Cr in the microstructure of the coatings are presented in Fig. 7. The content of both Zr and Cr elements in the coating composition increases with the increased levels of ZrO_2 nanoparticles in the bath up to 10 g/L, followed by a decrease in the content of the elements at higher ZrO_2 loading. The included ZrO_2 nanoparticles contribute to the reduction of chromium from its salt, i.e., $CrCl_3.6H_2O$; Therefore, it is not surprising to see a direct relationship between the content of Zr and Cr in the chemical composition of the nanocomposite layers. On the other hand, a higher loading of ZrO_2 in the bath increases the codeposition possibility of nanoparticles surrounded by the Ni^{2+} and Cr^{3+} cations as per the Guglielmi's model [60]. Thus, a higher amount of the nanoparticles will be incorporated into the growing Ni-Cr alloy deposit. The reason why Ni-Cr-20Z has less Zr content than Ni-Cr-10Z can be ascribed to the agglomeration of the nanoparticles, as shown in Fig. 4l).
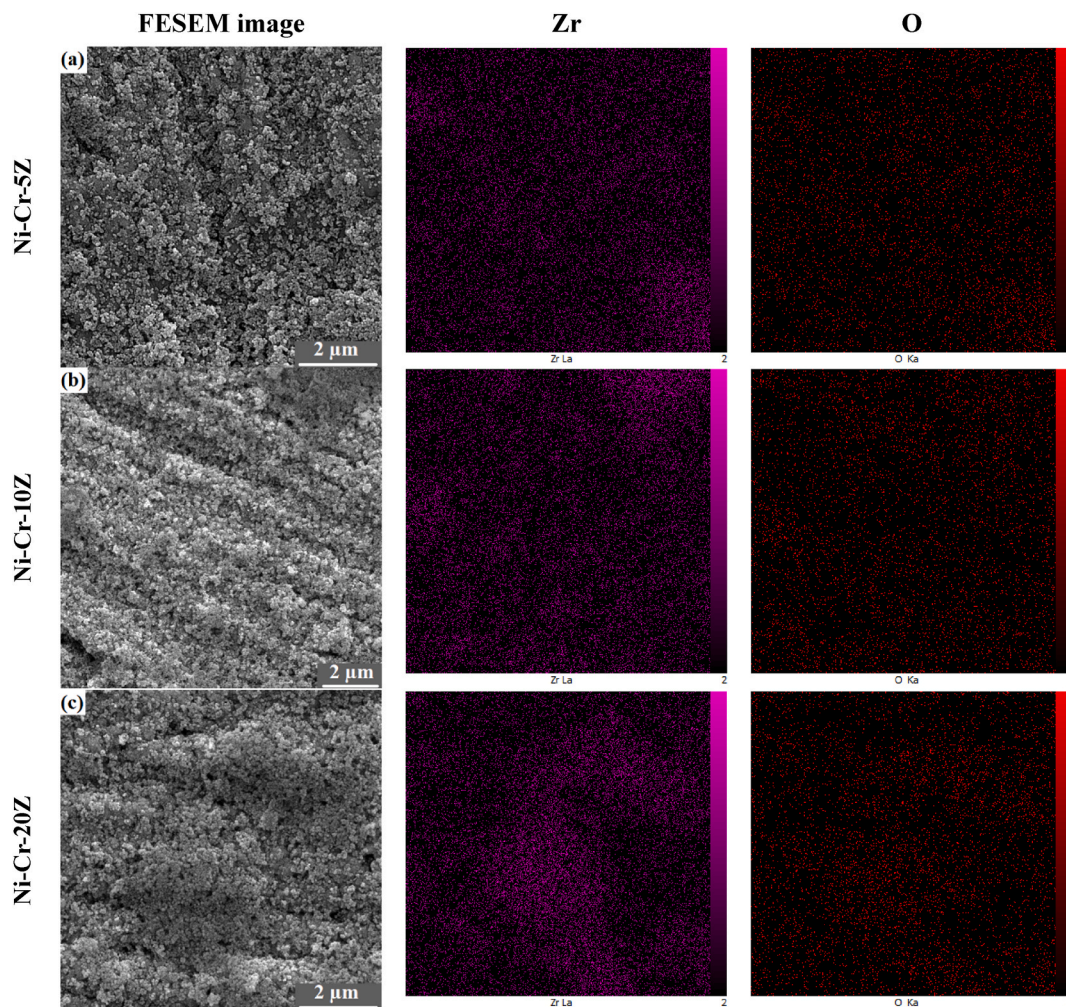

Fig. 5. EDS elemental mapping images of the Zr and O throughout the surface of composite layers: (a) Ni-Cr-5Z, (b) Ni-Cr-10Z, and (c) Ni-Cr-20Z.
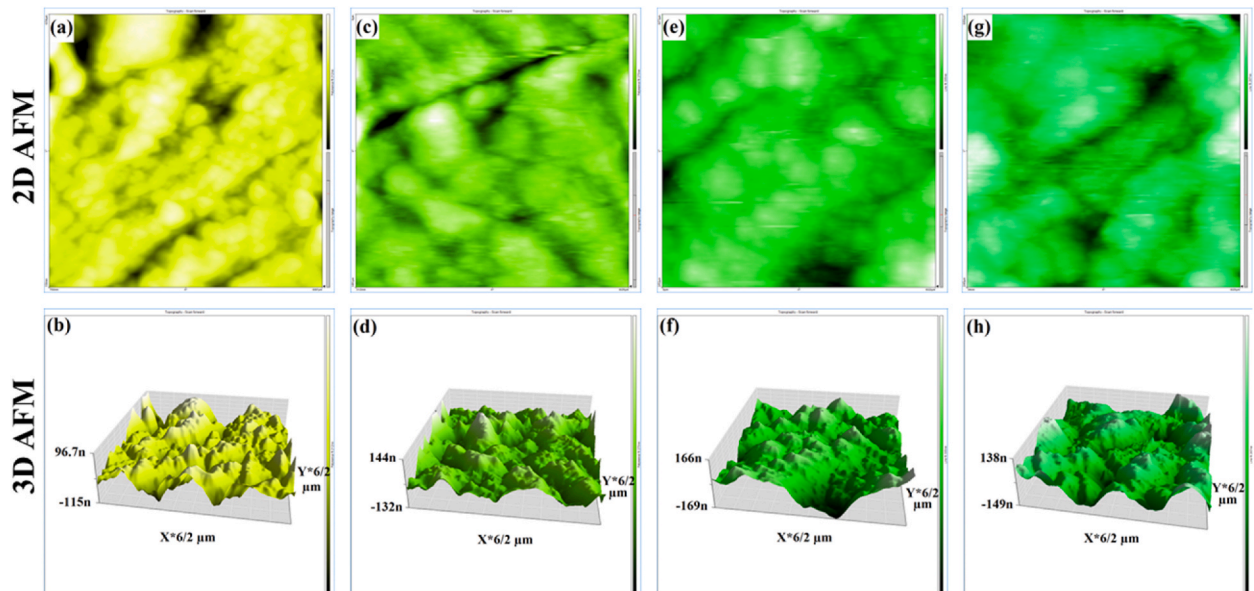
2D AFM

3D AFM

Fig. 6. The 2D and 3D AFM images of the samples: (a,b) Ni-Cr, (c,d) Ni-Cr-5Z, and (e,f) Ni-Cr-10Z and (g,h) Ni-Cr-20Z.

Table 4
Surface roughness (S_a) and root-mean-square roughness (S_q) values of the layers obtained by elaborating AFM data.

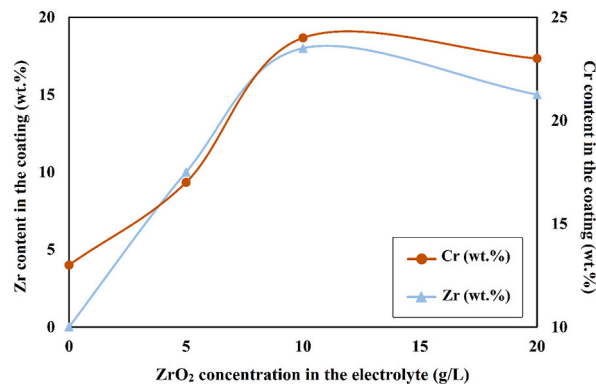| Coating type	S_a (nm)	S_q (nm)
Ni-Cr	26	35
Ni-Cr-5Z	37	48
Ni-Cr-10Z	48	62
Ni-Cr-20Z	52	68

Fig. 7. Changes in the content of Zr and Cr in the microstructure of the coatings electrodeposited from the electrolytes containing various amounts of the ZrO_2 nanoparticles.

3.5. Microhardness

The microhardness values of the specimens are provided in Fig. 8. The nanocomposite layers possess higher microhardness than that of alloy one, irrespective of the ZrO_2 nanoparticles loadings in the plating bath. The highest microhardness value is obtained when 10 g/L of the nanoparticles is added to the electrolyte, i.e., $\approx$35 % higher than the microhardness of the Ni-Cr. The potential mechanisms interpreting the microhardness improvement with the included ZrO_2 nanoparticles can be summarized as follows: (i) dispersion of the closely-spaced hard nanoparticles all over the Ni-Cr matrix, namely Orowan strengthening effect, which is shown in Figs. 4 and 5. The distributed nanoparticles can impede the movement of the dislocations; (ii) A decrease in crystallite size in agreement the Hall-
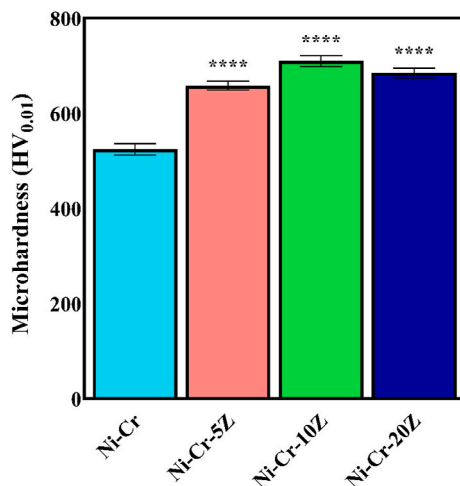
Fig. 8. Microhardness values of the alloy and nanocomposite electrodeposits (****$p < 0.0001$ *vs.* Ni-Cr).

Petch equation (Table 3); (iii) Increased content of the Cr in the chemical composition of the coatings, leading to a more pronounced solid-solution strengthening (Fig. 7). Since the Cr is harder than the Ni, an increase in Cr can promote the microhardness; and (iv) The formation of a more uniform and homogeneous surface [30,31,43,49,61]. The poor surface properties, as well as possessing lower Zr and Cr contents, are responsible for the lower microhardness of Ni-Cr-20Z compared to Ni-Cr-10Z. Demir et al. [48] electrodeposited Ni-Cr and Ni-Cr-hBN film on mild carbon steel, and assessed the influence of the hBN phase content on the mechanical properties of the coatings. They reported an improvement in the microhardness of the Ni-Cr film from 308 to 538 HV by the inclusion of hBN (up to 20 g/L). They observed a noticeable decrease in microhardness value, i.e., ≈80 HV, with an increase in hBN loadings to 30 g/L due to the agglomeration of the nanoparticles.

3.6. Corrosion performance

Fig. 9 presents the OCP-time curves of the films studied in 3.5 % (w/v) NaCl solution. There is a opposite trend between the changes of OCP-time curves of nanocomposite coatings and that of alloy layer. Moreover, the nanocomposite layers show more positive OCP values, which is an indicator of their lower tendency to corrode from the viewpoint of thermodynamics. The favorable condition for further EIS and PDP tests is obtained since OCP-time curves are stable in the range of 500–600 s.

The experimentally obtained Nyquist curves of the electrodeposits and EEC model used for analyzing the curves are illustrated in Fig. 10a) and Fig. 10b), respectively. Furthermore, the quantitative values of the EEC components are registered in Table 5. The
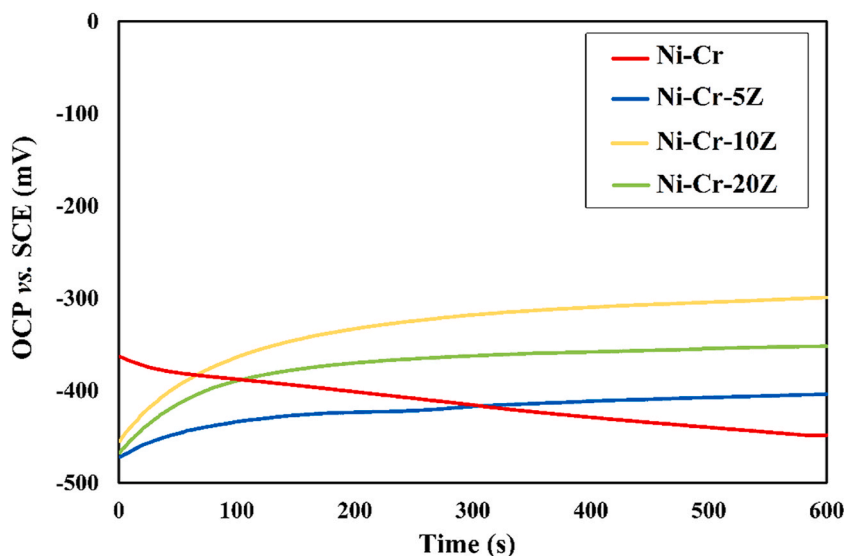

Fig. 9. The OCP-time curves of the Ni-Cr-based electrodeposits in 3.5 % (w/v) NaCl solution at 25.0 ± 1 °C.

incorporation of the reinforcing ZrO_2 phase into the Ni-Cr coatings leads to an increase in the values of R_{coat} and R_{ct}, corresponding to the improved corrosion protection efficiency of the nanocomposite coatings compared to the alloy one. The enhanced Q_c-n value is assigned to the more compact microstructure [12]. So, the data presented in Table 5 shows the formation of more compact coatings with the included ZrO_2 phase, which is in great compliance with the FESEM images. Moreover, the lower the Q_{dl} value, the thicker the double layer form on the material. Thus, the lower Q-Y0 value of the nanocomposite coatings is a marker of their superior corrosion resistance due to the generation of a thicker electrical double layer [1]. The chi-squared criterium (χ^2) values less than 0.001 indicate the favorable fitting [12].

The anti-corrosion behavior of a coating is dependent on surface and microstructural factors, including surface density, defects, topography, roughness, chemical composition, and homogeneity, as well as grain size and crystallinity. For particle-reinforced coatings, the content and dispersion of the particles should also be taken into consideration [61,62]. The parameters involved in a significant rise in anti-corrosion performance of the ZrO_2-reinforced Ni-Cr coatings, especially Ni-Cr-10Z, are as follows: (i) the more compact, defect-less and uniform surface, which prevents the diffusion of the corrosive medium toward the steel substrate; (ii) Excellent dispersion of the ceramic inert nanoparticles throughout the alloy matrix, where the nanoparticles serve as physical barriers against the brine medium; (iii) the increased Cr content, which renders high corrosion protection [30,48,61]. A higher surface roughness, surface defects, and possessing lower Cr and Zr contents are potential factors that led to a decrease in the corrosion performance of Ni-Cr-20Z. Bahrami Mousavi et al. [32] attempted to evaluate the influence of Cr and TiO_2 contents on the corrosion performance of the Ni-Cr-TiO_2 composite electrodeposits. They illustrated the direct relationship between the Cr and TiO_2 contents in the coatings and their polarization resistance (R_p) so that the highest corrosion resistance was obtained for Ni-15%Cr-7.1%TiO_2 film, ≈7 times higher than that of Ni-11.2%Cr.

Semilogarithmic potentiodynamic polarization plots of the specimens studied are exhibited in Fig. 11. The corrosion data derived from the plots are summarized in Table 6. The plots are in the active region, and there is a shift toward more negative current densities and more positive corrosion potential values with the included ZrO_2 reinforcing agents. The polarization resistance (R_p) is determined using the Stern-Geary equation provided elsewhere [12].

The lower the i_{corr} value, the slower the corrosion rate is. i_{corr} refers to the kinetic aspects of corrosion and is the most predominant parameter affecting the corrosion resistance of the given material [63]. The Ni-Cr-10Z coating, rendering the highest R_p and lowest
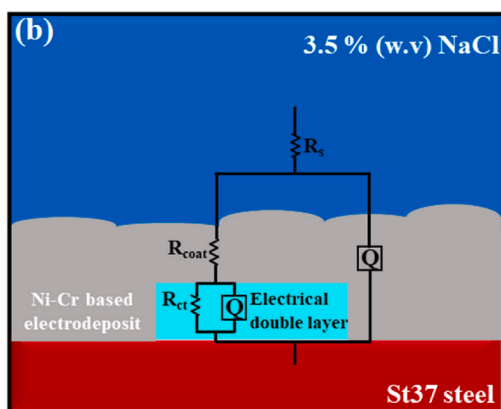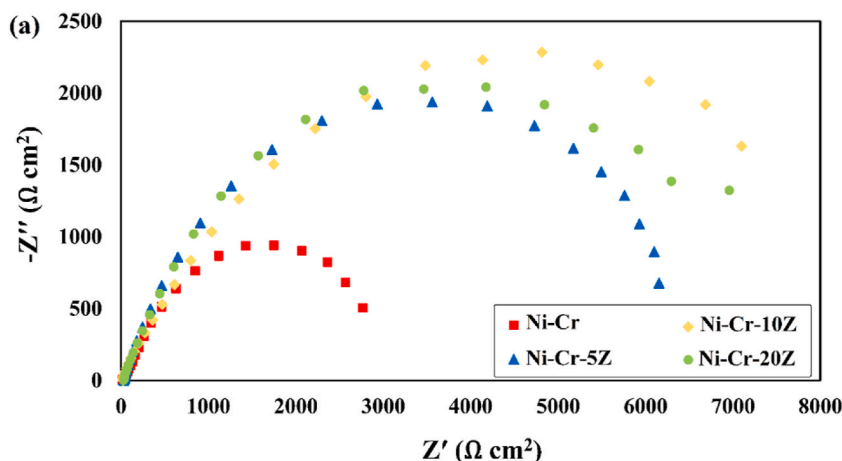

Fig. 10. (a) Experimentally obtained Nyquist curves of the electrodeposits and (b) EEC model used for analyzing the curves.

Table 5
The quantitative values of the EEC components. R_s, R_{coat}, R_{ct}, and Q are solution resistance, coating resistance, charge-transfer resistance, and constant phase element, respectively.

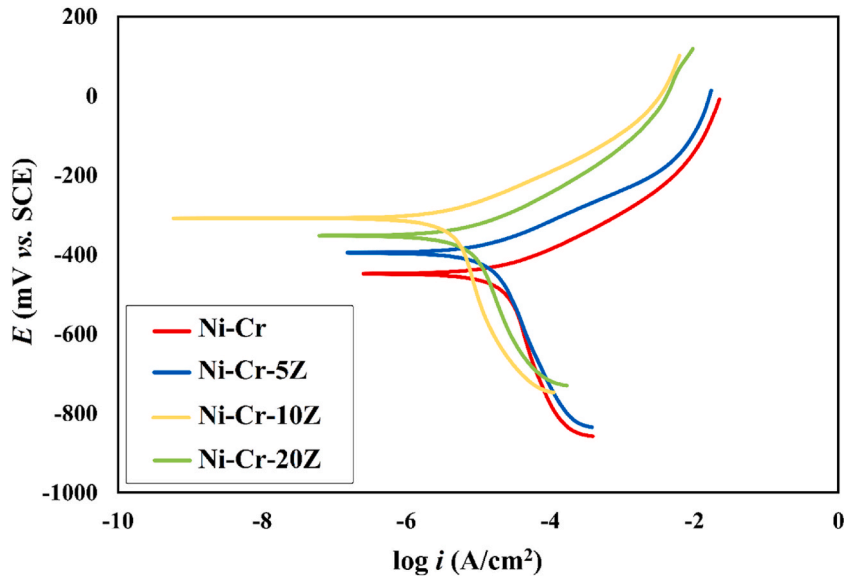| Coating type	R_s (Ω)	Q_c-Y0 (Ω^{-1} s^n cm^{-2})	Q_c-n	R_{coat} (Ω cm^2)	Q_{dl}-Y0 (Ω^{-1} s^n cm^{-2})	Q_{dl}-n	R_{ct} (Ω cm^2)	Fitting χ^2 value
Ni-Cr	6.4	3.7E-6	0.62	230	6E-4	0.73	3153	0.0003
Ni-Cr-5Z	7	2.3E-6	0.75	416	5.2E-4	0.76	6522	0.0002
Ni-Cr-10Z	7	1.1E-6	0.80	552	2.7E-4	0.82	8915	0.0002
Ni-Cr-20Z	8.2	1.7E-6	0.77	527	3.2E-4	0.80	7468	0.0004

Fig. 11. Semilogarithmic potentiodynamic polarization plots of the specimens studied.

Table 6
The corrosion data derived from the potentiodynamic polarization plots. i_{corr}, E_{corr}, β_a, and β_c, are corrosion current density, corrosion potential, anodic Tafel slope, and cathodic Tafel slope, respectively.

Coating type	E_{corr} (mV)	i_{corr} (μA/cm^2)	β_a (mV/decade)	β_c (mV/decade)	R_p (kΩ)
Ni-Cr	−448	15.84	51	−315	1203
Ni-Cr-5Z	−395	9.77	60	−311	2235
Ni-Cr-10Z	−308	3.13	70	−345	8074
Ni-Cr-20Z	−352	4.45	67	−300	5344

i_{corr}, possesses the best corrosion protection performance. Overall, the PDP results are in agreement with those obtained by EIS.

The possible anodic and cathodic half-cell reactions are as follows:

Cathodic reactions

$$2H^+ + 2e\text{-} = H_2 \tag{8}$$

$$O_2 + 4H^+ + 4e\text{-} = 2H_2O \tag{9}$$

Anodic reactions

$$Ni - 2e\text{-} = Ni2+ \tag{10}$$

$$Cr - 3e\text{-} = Cr^{3+} \tag{11}$$
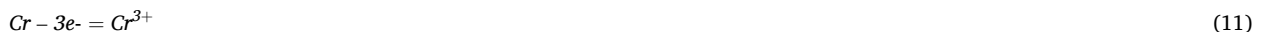
3.6.1. Weight loss

Table 7 outlines the corrosion-induced weight loss of the coatings submerged in 3.5 % (w/v) NaCl for 14 days. The lower weight

loss of the nanocomposite electrodeposits compared to the Ni-Cr layer is a sign of their superior corrosion protection. The Ni-Cr-10Z layer renders the lowest corrosion-induced weight loss due to its higher corrosion resistance, originating from the favorable morphological and microstructural features discussed earlier.

3.6.2. Morphology of the corroded surfaces

The FESEM images of the coatings after the destructive PDP test are presented in Fig. 12. As can be seen, the corrosion mechanism in all of the coatings studied is uniform corrosion. In other words, there is no sign of pitting and/or localized corrosion, and the surfaces are uniformly degraded by the corrosion medium. The morphology of the grains in Ni-Cr coating is changed from nodular and polyhedral to branched-like ones as a result of corrosion attacks (see Fig. 12a and b). The same phenomenon is observed for the nanocomposite layers (Fig. 12 c, d, g, and h) except for Ni-Cr-10Z coating, which preserved its initial morphology, as shown in Fig. 12e and f. This can be ascribed to the superior anti-corrosion properties of the Ni-Cr-10Z.

3.7. Tribological properties

Fig. 13 displays the COF-distance diagrams of the films. The mean COF values obtained are summarized in Table 8. The diagrams shown in Fig. 13a–d consist of two distinct areas, i.e., running-in and steady state. The running-in area, a period in which the pin slides over the surface, can be observed in the range of 0–20 m of the sliding. Then, the steady state appears, which corresponds to plastic deformation originating from the stress concentration [64].

The results confirmed the decrease in COF of the Ni-Cr layer, up to 42 %, when the ZrO_2 reinforcing phase is included. The lubricating action of the ZrO_2 nanoparticles is the major factor that leads to the lower COF values of the nanocomposite coatings compared to the Ni-Cr [65,66]. The simultaneous effects of the decreased COF and increased microhardness (according to the Archard's law) ensured the superior wear resistance of the ZrO_2-reinforced coatings [1]. Sheibani Aghdam et al. [31] evaluated the tribological properties of the Ni-Cr layer electrodeposited from Ni (II)-Cr(III) sulfate bath using the ball-on-disk technique at a load of 2N. The reported results illustrated that the COF of the coating is in the range of 0.46–0.75, depending on the Cr content of the coatings.

The wear-induced mass loss of the samples studied is shown in Fig. 14. A substantial decrease, up to 50 %, in the wear-induced mass loss of the Ni-Cr with the inclusion of the ZrO_2 further confirms the favorable wear resistance of these films.

4. Conclusions

The stress of present contribution was put on evaluating the influences of processing parameters, including current density, duty cycle, and ZrO_2 nanoparticles level in the electrolyte, on the mechano-corrosion and tribological properties of the Ni-Cr alloy electrodeposits. The important conclusions of the present work are listed as follows.

(i) The influence of current density and duty cycle on the microhardness of the Ni-Cu layers assessed before studying the role of the included ZrO_2 nanoparticles on the overall performance of the layers. The Ni-Cr layers electrodeposited under the current density of 8 A/dm^2 and current density of 60 % had the highest microhardness.

(ii) The included ZrO_2 nanoparticles led to a more compact and rougher surface containing finer crystallite. Moreover, there are lower surface defects over the surface of the nanocomposite coatings compared to that of the alloy coating.

(iii) The introduction of ZrO_2 nanoparticles to the Ni-Cr matrix positively contributed to the enhanced tribomechanical performance, where the Ni-Cr-10Z layer showed the highest microhardness and the lowest COF values.

(iv) Ni-Cr electrodeposit strengthened by 10 g/L of ZrO_2 nanoparticles rendered the strongest protection against the 3.5 % (w/v) NaCl corrosive medium. The post-corrosion morphology of the samples confirmed that the dominant corrosion mechanism was uniform corrosion.

(v) Ni-Cr-10Z electrodeposit provided the best anti-corrosion and tribomechanical properties, so, it can be considered a potential coating material for protection of St37 steel in severe service condition. The results highlighted the importance of inclusion of optimum concentration of the reinforcing nanoparticles in the coatings rather than excessive amounts.

(vi) The successful electrodeposition of Ni-Cr based coatings from the Ni(II)-Cr(III) bath requires precise control on the process parameters and the use of appropriate complexing agents. Progress in the final performance of these coatings in the near future requires exploiting the benefits of various reinforcing phase(s), different electrodeposition techniques, and control process factors.

Table 7
Corrosion-induced weight loss of the coatings immersed in 3.5 % (w/v) NaCl solution at 25.0 ± 1 °C for 14 days.

Coating type	Weight loss $(\frac{W_i - W_f}{W_i}) \times 100$
Ni-Cr	0.78 %
Ni-Cr-5Z	0.42 %
Ni-Cr-10Z	0.23 %
Ni-Cr-20Z	0.31 %
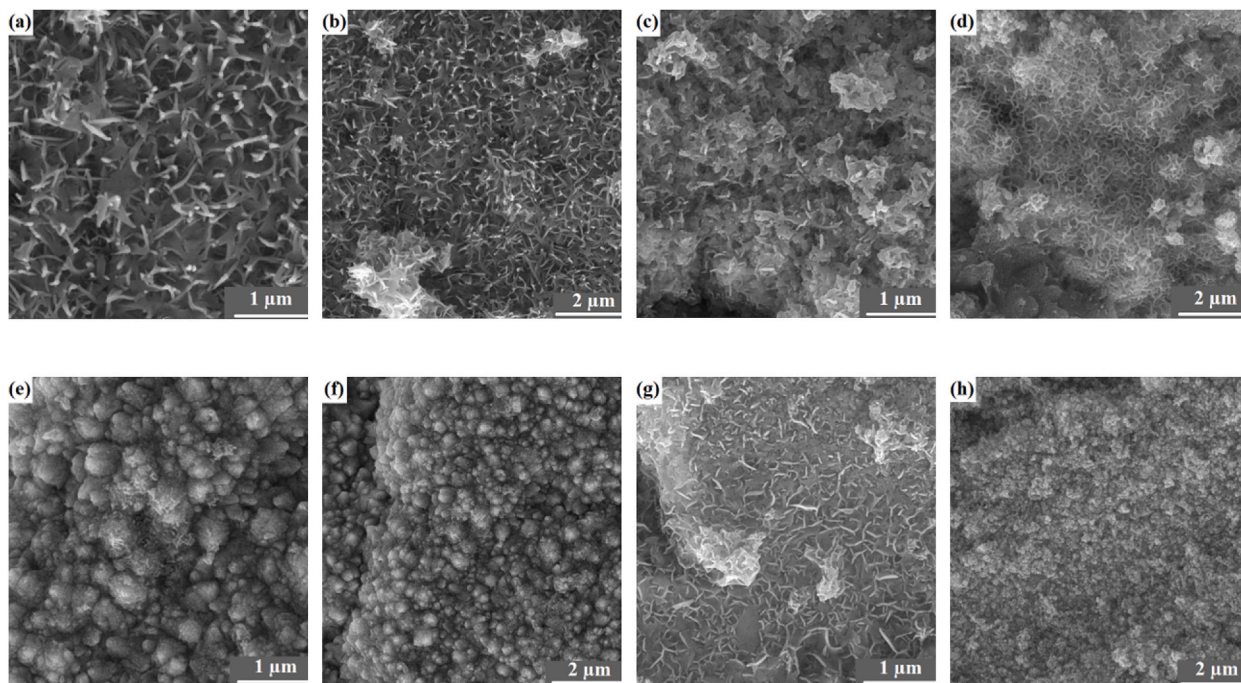
**Fig. 12.** FESEM images of the coatings after destructive PDP test within the potential range of −300 to 400 mV *vs.* the OCP: (a,b) Ni-Cr, (c,d) Ni-Cr-5Z, and (e,f) Ni-Cr-10Z and (g,h) Ni-Cr-20Z.
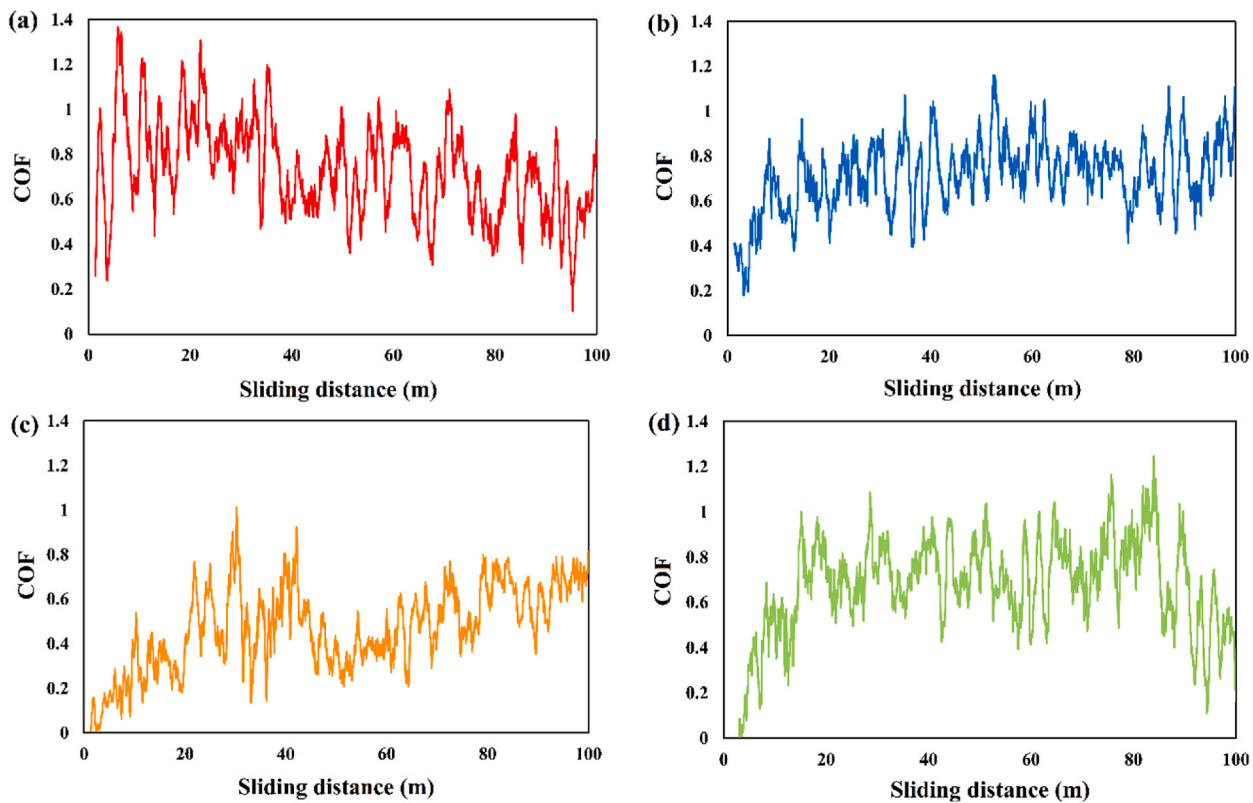
Fig. 13. The COF-distance diagrams of the Ni-Cr-based electrodeposits: (a) Ni-Cr, (b) Ni-Cr-5Z, and (c) Ni-Cr-10Z and (d) Ni-Cr-20Z.

Table 8
Mean COF values calculated using the COF-distance diagrams.

Coating type	Mean COF value
Ni-Cr	0.82
Ni-Cr-5Z	0.71
Ni-Cr-10Z	0.47
Ni-Cr-20Z	0.65
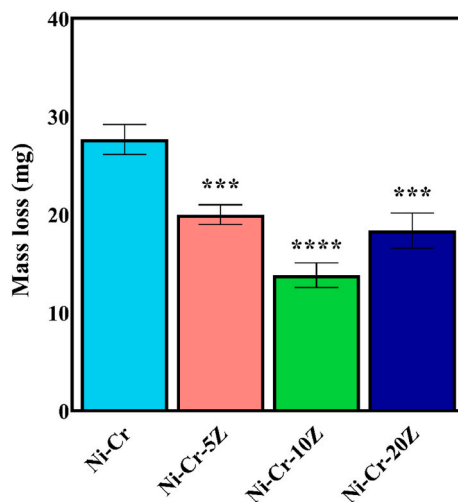
Fig. 14. Wear-induced mass loss of the samples studied (****$p < 0.0001$ and ***$p < 0.0005$ *vs.* Ni-Cr).

Data availability statement

The authors do not have permission to share data.

CRediT authorship contribution statement

Mir Saman Safavi: Writing – review & editing, Writing – original draft, Validation, Resources, Project administration, Methodology, Investigation, Formal analysis, Data curation. **Sima Soleimanzadeh Ghazijahani:** Resources, Investigation, Conceptualization. **Ali Rasooli:** Supervision.

Declaration of competing interest

The authors declare that they have no known competing financial interests or personal relationships that could have appeared to influence the work reported in this paper.

Abbreviations

AFM	Atomic force microscopy
COF	Coefficient of friction
EDL	Electrical double layer
EDS	Energy dispersive spectrometry
EEC	Electrical equivalent circuit
EIS	Electrochemical impedance spectroscopy
FCC	Face-centered-cubic
FESEM	Field emission scanning electron microscopy
FWHM	Full width at half maximum
OCP	Open circuit potential
PDP	Potentiodynamic polarization
XRD	X-ray diffraction

Appendix

Term	Definition
Coefficient of friction	The force that resists against the motion of two surfaces, which are under the vertical force.
Corrosion	A spontaneous/irreversible process in which electrochemical reactions between materials and substances in their environment results in chemical deterioration of the materials.
Current density	The amount of electric current passing over the unit cross-section area.
Duty cycle	Proportion of t_{on} compared to the total time.
Pin-on-disk test	A laboratory technique used to assess the tribological properties of the specimen.
Potentiodynamic polarization	An electrochemical technique where the potential is varied with time in a linear way while the current is recorded.
Tribology	The interdisciplinary science of understanding friction, lubrication, and wear phenomena for surfaces that are in relative motion.
XRD	A laboratory technique capable of determining structural information, such as crystal structure.

References

[1] M.S. Safavi, A. Rasooli, The positive contribution of Cr_2O_3 reinforcing nanoparticles to enhanced corrosion and tribomechanical performance of Ni–Mo alloy layers electrodeposited from a citrate-sulfate bath, J. Mater. Res. Technol. 28 (2024) 865–878.

[2] D.C. Lou, O.M. Akselsen, M.I. Onsøien, J.K. Solberg, J. Berget, Surface modification of steel and cast iron to improve corrosion resistance in molten aluminium, Surf. Coat. Technol. 200 (2006) 5282–5288.

[3] P. Abraha, Y. Yoshikawa, Y. Katayama, Surface modification of steel surfaces by electron beam excited plasma processing, Vacuum 83 (2008) 497–500.

[4] B. Vasudevan, L. Nagarajan, L. Natrayan, A. Karthick, S.K. Mahalingam, C. Prakash, C.K. Chan, H. Panchal, M.I. Siddiqui, Experimental study, modeling, and parametric optimization on abrasive waterjet drilling of YSZ-coated Inconel 718 superalloy, J. Mater. Res. Technol. 29 (2024) 4662–4675.

[5] S.V. Wagh, S.R. More, V.V. Madhav, K.K. Saxena, D. Bandhu, B.D. Sunil, V. Revathi, M.I. Siddiqui, Effects of low-power laser hardening on the mechanical and metallurgical properties of biocompatible SAE 420 steel, J. Mater. Res. Technol. 30 (2024) 1611–1619.

[6] M.S. Safavi, M.A. Surmeneva, R.A. Surmenev, J. Khalil-Allafi, RF-magnetron sputter deposited hydroxyapatite-based composite & multilayer coatings: a systematic review from mechanical, corrosion, and biological points of view, Ceram. Int. 47 (2021) 3031–3053.

[7] M.S. Safavi, F.C. Walsh, M.A. Surmeneva, R.A. Surmenev, J. Khalil-Allafi, Electrodeposited hydroxyapatite-based biocoatings: recent progress and future challenges, Coatings 11 (2021) 110.

[8] A. Zanurin, N.A. Johari, J. Alias, H.M. Ayu, N. Redzuan, S. Izman, Research progress of sol-gel ceramic coating: a review, Mater. Today Proc. 48 (2022) 1849–1854.

[9] B. Fotovvati, N. Namdari, A. Dehghanghadikolaei, On coating techniques for surface protection: a review, J. Manuf. Mater. Process. 3 (2019) 28.

[10] S. Kumar, M. Kumar, A. Handa, Erosion corrosion behaviour and mechanical properties of wire arc sprayed Ni-Cr and Ni-Al coating on boiler steels in a real boiler environment, Mater. High Temp. 37 (2020) 370–384.

[11] A. Mazouzi, A. Rezzoug, B. Cheniti, S.E. Lebouachera, D. Miroud, A.R. Boukantar, N. Drouiche, B. Djerdjare, Impact of wear parameters on NiCr-WC10Co4Cr and WC10Co4Cr HVOF sprayed composite coatings using response surface methodology, Int. J. Adv. Manuf. Technol. 114 (2021) 525–539.

[12] M.S. Safavi, J. Khalil-Allafi, I. Ahadzadeh, F.C. Walsh, L. Visai, Improved corrosion protection of a NiTi implant by an electrodeposited HAp-Nb_2O_5 composite layer, Surf. Coat. Technol. 470 (2023) 129822.

[13] M.S. Safavi, J. Khalil-Allafi, E. Restivo, A. Ghalandarzadeh, M. Hosseini, G. Dacarro, L. Malavasi, A. Milella, A. Listorti, L. Visai, Enhanced in vitro immersion behavior and antibacterial activity of NiTi orthopedic biomaterial by HAp- Nb_2O_5 composite deposits, Sci. Rep. 13 (2023) 16045.

[14] A.A. Ojo, I.M. Dharmadasa, Electroplating of semiconductor materials for applications in large area electronics: a review, Coatings 8 (2018) 262.

[15] S. Awasthi, S. De, S.K. Pandey, Electrodeposited carbon nanostructured nickel composite coatings: a review, Heliyon 10 (2024) e26051.

[16] V.S. Protsenko, L.S. Bobrova, T.E. Butyrina, A.S. Baskevich, S.A. Korniy, F.I. Danilov, Electrodeposited Ni–Mo coatings as electrocatalytic materials for green hydrogen production, Heliyon 9 (2023) e15230.

[17] U.P. Kumar, S. Shanmugan, C.J. Kennady, S.M. Shibli, Anti-corrosion and microstructural properties of Ni–W alloy coatings: effect of 3, 4-Dihydroxybenzaldehyde, Heliyon 5 (2019) e01288.

[18] C. Oulmas, S. Mameri, D. Boughrara, A. Kadri, J. Delhalle, Z. Mekhalif, B. Benfedda, Comparative study of Cu–Zn coatings electrodeposited from sulphate and chloride baths, Heliyon 5 (2019) e02058.

[19] B.O. Okonkwo, C. Jeong, H.B. Lee, C. Jang, E. Rahimi, A. Davoodi, Development and optimization of trivalent chromium electrodeposit on 304L stainless steel to improve corrosion resistance in chloride-containing environment, Heliyon 9 (2023) e22538.

[20] M.S. Safavi, M. Fathi, I. Ahadzadeh, Feasible strategies for promoting the mechano-corrosion performance of Ni–Co based coatings: which one is better? Surf. Coat. Technol. 420 (2021) 127337.

[21] A. Rasooli, M.S. Safavi, F. Babaei, A. Ansarian, Electrodeposited Ni–Fe–Cr_2O_3 nanocomposite coatings: a survey of influences of Cr_2O_3 nanoparticles loadings in the electrolyte, J. Alloys Compd. 822 (2020) 153725.

[22] A. Rasooli, M.S. Safavi, S. Ahmadiyeh, A. Jalali, Evaluation of TiO_2 nanoparticles concentration and applied current density role in determination of microstructural, mechanical, and corrosion properties of Ni–Co alloy coatings, Prot. Met. Phys. Chem. Surf. 56 (2020) 320–327.

[23] M.S. Safavi, A. Rasooli, F.A. Sorkhabi, Electrodeposition of Ni-P/Ni-Co-Al_2O_3 duplex nanocomposite coatings: towards improved mechanical and corrosion properties, Trans. IMF 98 (2020) 320–327.

[24] N.S. Mbugua, M. Kang, Y. Zhang, N.J. Ndiithi, G.V. Bertrand, L. Yao L, Electrochemical deposition of Ni, NiCo alloy and NiCo–ceramic composite coatings—a critical review, Materials 13 (2020) 3475.

[25] Y. Li, X. Cai, G. Zhang, C. Xu, W. Guo, M. An, Optimization of electrodeposition nanocrytalline Ni-Fe alloy coatings for the replacement of Ni coatings, J. Alloys Compd. 903 (2022) 163761.

[26] X. Fu, F. Wang, X. Chen, J. Lin, H. Cao, Corrosion resistance of Ni–P/SiC and Ni–P composite coatings prepared by magnetic field-enhanced jet electrodeposition, RSC Adv. 10 (2020) 34167–34176.

[27] A. Niciejewska, A. Ajmal, M. Pawlyta, M. Marczewski, J. Winiarski, Electrodeposition of Ni–Mo alloy coatings from choline chloride and propylene glycol deep eutectic solvent plating bath, Sci. Rep. 12 (2022) 18531.

[28] A. Ren, M. Kang, X. Fu, Corrosion behaviour of Ni/WC-MoS_2 composite coatings prepared by jet electrodeposition with different MoS_2 doping concentrations, Appl. Surf. Sci. 613 (2023) 155905.

[29] H. Zhang, L. Liu, J. Bai, X. Liu, Corrosion behavior and microstructure of electrodeposited nano-layered Ni–Cr coatings, Thin Solid Films 595 (2015) 36–40.

[30] H. Firouzi-Nerbin, F. Nasirpouri, E. Moslehifard, Pulse electrodeposition and corrosion properties of nanocrystalline nickel-chromium alloy coatings on copper substrate, J. Alloys Compd. 822 (2020) 153712.

[31] A.S. Aghdam, S.R. Allahkaram, S. Mahdavi, Corrosion and tribological behavior of Ni–Cr alloy coatings electrodeposited on low carbon steel in Cr (III)–Ni (II) bath, Surf. Coat. Technol. 281 (2015) 144–149.

[32] A. Bahrami Mousavi, P. Baghery, M. Peikari, G.R. Rashed, Preparation and characterization of Ni-Cr nanocomposite coatings containing TiO$_2$ nanoparticles for corrosion protection, Anti-Corrosion Method, Mater 59 (2012) 279–284.

[33] Z. Dong, X. Peng, Y. Guan, L. Li, F. Wang, Optimization of composition and structure of electrodeposited Ni–Cr composites for increasing the oxidation resistance, Corros. Sci. 62 (2012) 147–152.

[34] Y. Zhang, X. Peng, F. Wang, Development and oxidation at 800 C of a novel electrodeposited Ni–Cr nanocomposite film, Mater. Lett. 58 (2004) 1134–1138.

[35] M.S. Marwah, V. Srinivas, A.K. Pandey, S.R. Kumar, K. Biswas, J. Maity, Morphological changes during annealing of electrodeposited Ni-Cr coating on steel and their effect on corrosion in 3% of NaCl solution, J. Iron Steel Res. Int. 18 (2011) 72–78.

[36] W. Sassi, H. Boubaker, S. Bahar, M. Othman, A. Ghorbal, R. Zrelli, J.Y. Hihn, A challenge to succeed the electroplating of nanocomposite Ni–Cr alloy onto porous substrate under ultrasonic waves and from a continuous flow titanium nanofluids, J. Alloys Compd. 828 (2020) 154437.

[37] Y.B. Zhou, G.G. Zhao, H.J. Zhang, Fabrication and wear properties of co-deposited Ni-Cr nanocomposite coatings, Trans. Nonferrous Met. Soc. China 20 (2010) 104–109.

[38] Z. Razaghi, M. Rezaei, S.H. Tabaian, Electrochemical noise and impedance study on the corrosion of electroplated Ni-Cr coatings in HBF4 aqueous solution, J. Electroanal. Chem. 859 (2020) 113838.

[39] S. Jeyaraj, K.P. Arulshri, S. Ramesh, G. Muthukumaran, Experimental investigations and effects studies on electrodeposited Ni-Cr composite coating using robust design approach, Mater. Today Proc. 5 (2018) 6999–7008.

[40] J. Sun, D.X. Du, H.F. Lv, L. Zhou, Y.G. Wang, C.G. Qi, Microstructure and corrosion resistance of pulse electrodeposited Ni–Cr coatings, Surf. Eng. 31 (2015) 406–411.

[41] M.E. Bahrololoom, A. Hoveidaei, Influence of post-heat treatment and complexing agents on hardness of Ni–Cr alloy coatings, Surf. Eng. 15 (1999) 502–504.

[42] C.N. Tharamani, F.S. Hoor, N.S. Begum, S.M. Mayanna, Electrodeposition and characterization of Ni–Cr alloy coating, J. Electrochem. Soc. 153 (2006) C164.

[43] Y.F. Yang, Z.Q. Gong, L.Y. Deng, B.P. Luo, Y.T. Ma, Z.H. Yang, Electrodeposition of Ni-Cr alloy on aluminum substrate, J. Cent. South Univ. Technol. 13 (2006) 219–224.

[44] D. Khedekar, V. Gosavi, C. Gogte, P. Brahmankar, Optimization of process parameters of nickel–chromium electroplating for thickness variation using genetic algorithm, in: International Conference on Communication and Signal Processing (ICCASP 2016), December, Lonere, India, 2016, pp. 26–27.

[45] X. Peng, Y. Zhou, F.H. Wang, Y. Zhang, On the development and the oxidation of novel Ni-Cr and Ni-Al nanocoatings by composite electrodeposition, Mater. Sci. Forum 461 (2004) 409–416.

[46] L.J. Qin, Y.C. Huang, Electrochemical study of the effect of oxidation and amorphization of Cr nanoparticles on the co-deposition of Ni-Cr nanocomposite film, J. Electroanal. Chem. 795 (2017) 110–115.

[47] M.S. Safavi, J. Khalil-Allafi, A. Motallebzadeh, C. Volpini, V. Khalili, L. Visai, Encouraging tribomechanical and biological responses of hydroxyapatite coatings reinforced by various levels of niobium pentoxide particles, Mater. Adv. 4 (2023) 5618–5632.

[48] M. Demir, E. Kanca, I.H. Karahan, Characterization of electrodeposited Ni–Cr/hBN composite coatings, J. Alloys Compd. 844 (2020) 155511.

[49] T. Abedi, S.K. Asl, Synthesis of a novel functionally graded coatings of Ni-Cr/Al$_2$O$_3$ nanocomposite coating by pulse electrodeposition, Mater. Res. Express 6 (2019) 056403.

[50] J. Fan, T. Lin, F. Hu, Y. Yu, M. Ibrahim, R. Zheng, S. Huang, J. Ma, Effect of sintering temperature on microstructure and mechanical properties of zirconia-toughened alumina machinable dental ceramics, Ceram. Int. 43 (2017) 3647–3653.

[51] A.A. Madfa, F.A. Al-Sanabani, N.H. Al-Qudami, J.S. Al-Sanabani, A.G. Amran, Use of zirconia in dentistry: an overview, The Open Biomater. J. 5 (2014) 1–9.

[52] R.A. Shakoor, R. Kahraman, U.S. Waware, Y. Wang, W. Gao, Properties of electrodeposited Ni-B-ZrO$_2$ composite coatings, Int. J. Electrochem. Sci. 10 (2015) 2110–2119.

[53] Z. Fattahi, S.A. Sajjadi, A. Babakhani, F. Saba, Ni–Cr matrix composites reinforced with nano-and micron-sized surface-modified zirconia: synthesis, microstructure and mechanical properties, J. Alloys Compd. 817 (2020) 152755.

[54] N.M. Dawood, K.F. Al-Sultani, H.H. Jasim, Zhe role of zirconia additions on the microstructure and corrosion behavior of Ni-Cr dental alloys, Mater. Res. Express 8 (2021) 045404.

[55] M. Fathi, M.S. Safavi, A. Ansariyan, I. Ahadzadeh, A promising horizon in mechanical and corrosion properties improvement of Ni-Mo coatings through incorporation of Y$_2$O$_3$ nanoparticles, Metall. Mater. Trans. A 51 (2020) 897–908.

[56] M. Fathi, M.S. Safavi, S. Mahdavi, S. Mirzazadeh, V. Charkhesht, A. Mardanifar, M. Mehdipour, Co–P alloy matrix composite deposits reinforced by nano-MoS$_2$ solid lubricant: an alternative tribological coating to hard chromium coatings, Tribol. Int. 159 (2021) 106956.

[57] B.O. Okonkwo, C. Jeong, C. Jang, Advances on Cr and Ni electrodeposition for industrial applications—a Review, Coatings 12 (2022) 1555.

[58] Y.B. Song, D.T. Chin, Current efficiency and polarization behavior of trivalent chromium electrodeposition process, Electrochim. Acta 48 (2002) 349–356.

[59] C. Xu, B. Li, Z. Liu, Z. Yuan, Z. Zhang, S. Chen, Preparation of nanocrystalline Ni–Mo and Ni–Mo–ZrO$_2$ coating and investigation of its corrosion resistance and wear behaviors, Ceram. Int. 48 (2022) 37102–37113.

[60] C.T. Low, R.G. Wills, F.C. Walsh, Electrodeposition of composite coatings containing nanoparticles in a metal deposit, Surf. Coat. Technol. 201 (2006) 371–383.

[61] M.S. Safavi, F.C. Walsh, Electrodeposited Co-P alloy and composite coatings: a review of progress towards replacement of conventional hard chromium deposits, Surf. Coat. Technol. 422 (2021) 127564.

[62] M.S. Safavi, M. Tanhaei, M.F. Ahmadipour, R.G. Adli, S. Mahdavi, F.C. Walsh, Electrodeposited Ni-Co alloy-particle composite coatings: a comprehensive review, Surf. Coating. Technol. 382 (2020) 125153.

[63] X.L. Zhang, Z.H. Jiang, Z.P. Yao, Y. Song, Z.D. Wu, Effects of scan rate on the potentiodynamic polarization curve obtained to determine the Tafel slopes and corrosion current density, Corros. Sci. 51 (2009) 581–587.

[64] J.H. Liu, Y.D. Liu, Z.L. Pei, W.H. Li, W.B. Shi, J. Gong, C. Sun, Influence of particle size and content on the friction and wear behaviors of as-annealed Ni–Mo/diamond composite coatings, Wear 452 (2020) 203300.

[65] S. Ma, S. Zheng, D. Cao, H. Guo, Anti-wear and friction performance of ZrO$_2$ nanoparticles as lubricant additive, Particuology 8 (2010) 468–472.

[66] A. Rylski, K. Siczek, The effect of addition of nanoparticles, especially ZrO$_2$-based, on tribological behavior of lubricants, Lubricants 8 (2020) 23.